APPLIED SCIENCES AND ENGINEERING

A wearable triboelectric impedance tomography system for noninvasive and dynamic imaging of biological tissues

Peng Yang[1,2], Zhaoqi Liu[1,2], Siyao Qin[1,2], Jun Hu[1,2], Songmei Yuan[3], Zhong Lin Wang[1,2,4], Xiangyu Chen[1,2]*

Tissue imaging is usually captured by hospital-based nuclear magnetic resonance. Here, we present a wearable triboelectric impedance tomography (TIT) system for noninvasive imaging of various biological tissues. The imaging mechanism relies on the obtained impedance information from the different soft human tissues. A high-precision signal source is designed on the basis of a composite triboelectric nanogenerator, which exhibits a minimal total harmonic distortion of 0.03% and a peak output signal-to-noise ratio up to 120 decibels. The current density injected into human skin is around 79.58 milliamperes per square meter, far below the safety threshold for medical devices. The TIT system achieves time-resolved tomography of human limbs' soft tissues, and many appealing functions can be realized by using this wearable system, including the observation of muscle movement, the motion intention recognition, and the identification of pathological changes of soft tissue. Hence, this TIT system with excellent biocompatibility can be integrated with various devices, such as medical-assistive exoskeletons and smart protective suit.

INTRODUCTION

Imaging soft tissue within organisms holds notable promise for evaluating the prolonged physiological or pathological states, as well as for facilitating tailored clinical management and rehabilitation interventions of patients (*1*–*4*). Currently, the mainstream technique for noninvasive imaging, such as magnetic resonance imaging (MRI) and computed tomography (CT), encounter the limitations of excessive volume, heavy weight, high cost and high energy consumption, despite their advantages in detection accuracy (*5*–*11*). With the escalating demand for point-of-care testing, wearable human body monitoring technologies have garnered increasing attention on account of the characteristics of portability, lightweight construction, and customizable features (*12*–*15*). For example, ultrasound imaging devices targeting the heart and breast (*1*–*3*, *16*, *17*), along with magnetic induction tomography sensitive to intracranial hemorrhage (*18*–*20*), have been reported as typical wearable imaging device. Nonetheless, these devices also confront various challenges, including the coupling media intervention, signal distortion stemming from skin strain and so on (*4*, *21*–*23*). More importantly, due to the inherent differences in tissue composition and physiological states, it is difficult to achieve comprehensive, all-encompassing detection only by using one kind of wearable imaging device (*24*, *25*). Therefore, it is still quite necessary to keep developing wearable imaging devices based on diversified imaging mechanisms.

Electrical Impedance Tomography (EIT), used for reconstructing the spatial distribution of electrical properties within specific domains, also constitutes a distinctive research branch of biomedical imaging (*4*, *26*–*30*). Although the possibility of desktop-based EIT instruments for human organ monitoring has been validated by previous work, the development of wearable and potable EIT devices for dynamic tissue imaging still confronts several fundamental challenges, including the frequency-dependent internal resistance of the current source, cross-talk induced by device miniaturization, and parasitic capacitance effects (*31*–*35*). More importantly, high-quality imaging in EIT should be achieved by amplifying the current injection, while the excessive current stimulation on skin can also induce neurological or muscular damage (*36*–*38*). Hence, the image quality of EIT is relying on the low-noise and high-fidelity hardware design, with the primary difficulties lying in the preparation of a current source having outstanding load adaptability and signal quality. On the other hand, the triboelectric nanogenerator (TENG) technology has undergone remarkable development in the past decade (*39*–*44*). The intrinsic properties of ultralow current output and highly controllable transferred charges of TENG enable the emergence of various bioelectronic devices with superior biocompatibility (*45*–*50*). In this case, the combination of TENG electrostatic energy and imaging algorithm of impedance tomography may initiate a different strategy for wearable tomography system.

This work proposes a wearable triboelectric impedance tomography (TIT) technique for monitoring human soft tissues with detection current at microampere level. A high-precision electrostatic signal source (HESS) based on the composite TENG is designed for providing high-quality probing electrical signal with excellent biocompatibility for this TIT system, while the fine impedance analysis can be achieved with a current signal far below the safety standards for medical devices. The total harmonic distortion (THD) of HESS current reaches 0.03%, and its current variation rate drops to 0.01%. This signal quality has never been realized by the previously reported TENG device. On the basis of this TIT system, the wearable temporal imaging of human limb soft tissues is

[1]Beijing Key Laboratory of Micro-Nano Energy and Sensor, Center for High-Entropy Energy and Systems, Beijing Institute of Nanoenergy and Nanosystems, Chinese Academy of Sciences, Beijing 101400, P. R. China. [2]School of Nanoscience and Technology, University of Chinese Academy of Sciences, 100049 Beijing, China. [3]School of Mechanical Engineering and Automation, Beihang University, Beijing 100191, China. [4]Georgia Institute of Technology, Atlanta, GA 30332-0245, USA.
*Corresponding author. Email: chenxiangyu@binn.cas.cn

accomplished. The dynamic observation of muscle movement and motion intention identification in limb can be achieved, while the tiny abnormal lesions in deep tissues can also be distinguished by the cross-sectional image obtained from TIT device, such as microfracture. With superior biocompatibility and lightweight design, this TIT device can be integrated with medical-assistive exoskeletons or smart protective suit for diversified applications, including soft tissue kinematic analysis, deep lesion monitoring, and even rehabilitation treatments.

RESULTS

As depicted in Fig. 1A, this work introduces a TIT system for soft tissue imaging in limbs. From the hardware perspective, the TIT system is consisted of the HESS for signal generation, the electronic skin (e-skin) as the detector, and a microcontroller for data processing. The impedance feedback information, in response to injected current, is collected by e-skin, and the time-variant conductivity images of various soft tissue can be rapidly produced by data processing module. The impedance model of biological tissues, tailored to

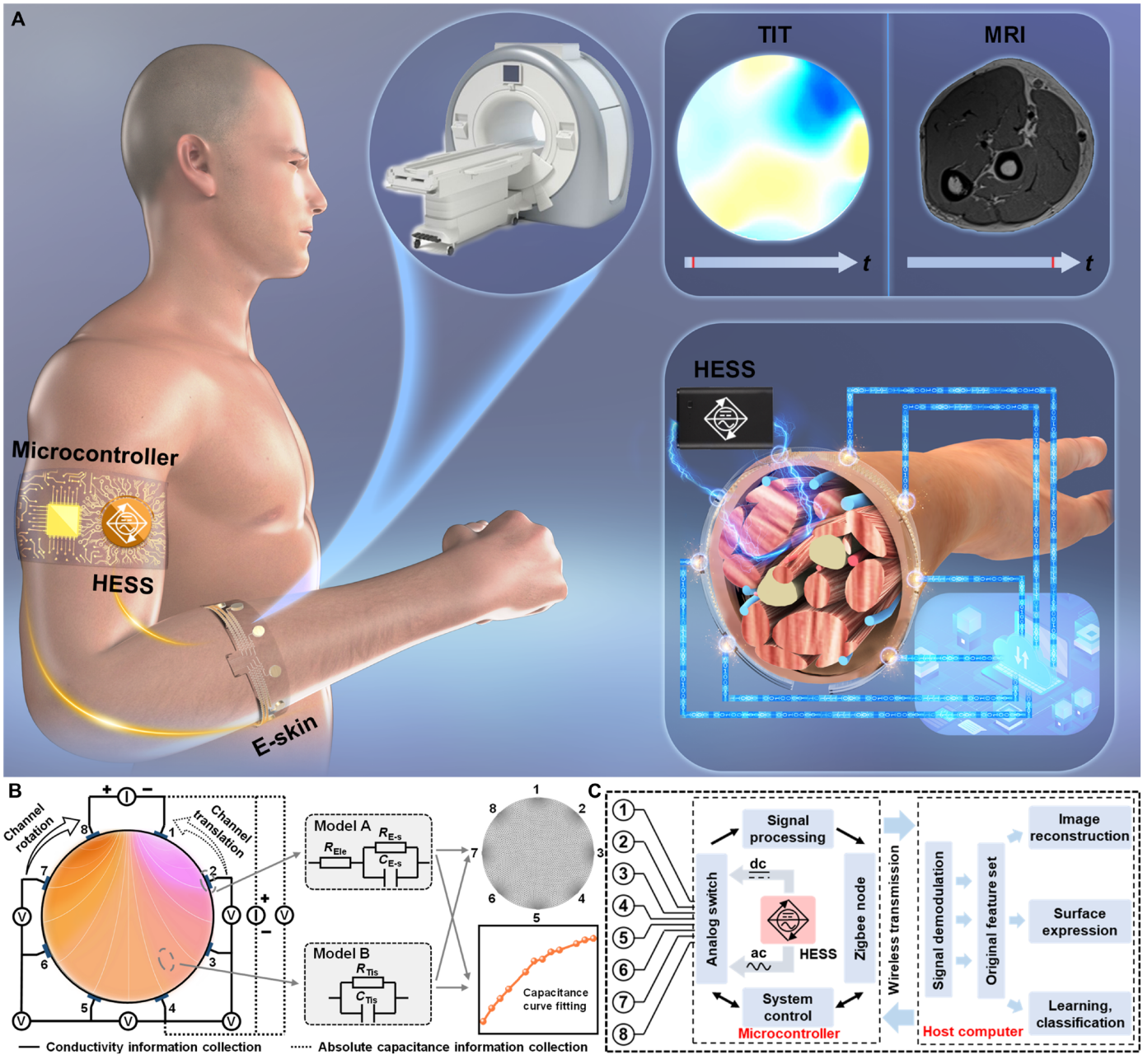

Fig. 1. Overview of the design scheme and system components for the TIT system for soft tissue imaging of limbs. (**A**) The design philosophy operational principles, and comparative analysis with imaging results of the TIT system. (**B**) Operational mode of TIT and the derivation of impedance models pertaining of human tissue, where "I" and "V" represent the controlled current source and the measuring voltmeter, respectively. (**C**) The comprehensive framework delineation and data processing strategies used in the TIT system.

the physiological structure of the human body, is crucial for image reconstruction. The impedance network is formed by the coupling connection between two fundamental impedance elements [electrode-skin (A) and internal tissues (B)] (Fig. 1B). As for impedance element A, the resistance ($R_{E\text{-}S}$) and capacitance ($C_{E\text{-}S}$) between the electrode-skin surfaces, as well as the electrode resistance (R_{Ele}), are decided by the contact conditions between the electrode and the skin. Impedance element B depicts the impedance of the internal soft tissue, where the resistance (R_{Tis}) and capacitance (C_{Tis}) of the tissue at the sensing location are related to the tissue type and state. Therefore, physiological or pathological variations in tissues alter the mentioned electrical parameters, causing changes in regional impedance, which can be mapped to boundary voltage. The four-terminal measurement mode, selecting two adjacent electrodes as current injection points and collecting voltage signals sequentially from all the other adjacent electrode pairs, is applied for the acquisition of conductivity information (Fig. 1B). By altering the current injection strategy and performing dc injection using a opposite electrode pair, the characteristic curve containing the absolute capacitance value of human tissue can also be obtained (Fig. 1B). The overall design scheme of the TIT system is illustrated in Fig. 1C, where eight electrodes are integrated onto the e-skin and interconnected via flexible circuits and a microcontroller. The processing of collected physiological information is primarily carried out on the host computer, achieving functions such as image reconstruction and machine learning–based classification.

The e-skin attached on human body for signal output and data acquisition is depicted in fig. S1, including a four-layer functional architecture—encapsulation layer, supporting layer, conductive network, and adhesive layer (see Materials and Methods and figs. S2 to S4 for preparation procedures), with the total thickness less than 10 μm. The patterned conductive network, including contact electrodes and serpentine transmission lines, are fabricated by poly(3,4-ethylenedioxythiophene):poly(styrenesulfonate) (PEDOT:PSS)-polyurethane-silver nanowires (AgNWs) (PPPA). The remaining three functional layers use the polyvinyl alcohol/chitosan (PVA/CS) solution as the foundational material, due to its exceptional biocompatibility and intrinsic antimicrobial attributes (*51*, *52*). Nevertheless, diverse treatment methods are implemented to accommodate the distinct functionalities across these layers, such as the hydrophobic treatment to the encapsulation layer (fig. S5). The e-skin on the human body can efficiently respond to mechanical deformations of the skin, and the modification of its key dimensional parameters allows adaptation to different subjects (fig. S6). Temperature is considered the critical factor for activating the adhesion layer, which is deemed fully activated only upon the completion of its phase transition. Therefore, the activation time of the adhesion layer can be equated to the phase transition time. Temperature-responsive analysis and thermal images of the PVA/CS solution reveals the negative correlation between the activation time of the adhesion layer and ambient temperature (Fig. 2A and fig. S7). The inset indicates an average activation time of 1 min for the adhesion layer on human skin, which can meet the requirements of wearable testing (Fig. 2A). The tensile strength, shear strength, and interfacial toughness between PVA/CS and porcine skin are 53.16 kPa, 72.76 kPa, and 2.49 J m^{-2}, respectively (fig. S8). The adhesion strength between the PVA/CS and porcine skin is enough to provide reliable adhesion within 500 min (fig. S9). Sweat secretion bring on influence to adhesion force, and this measurement is investigated through the independently designed simulated sweating device, as detailed in fig. S10 and note S1. Furthermore, the comparison of the breathability and long-term sensitization assessment of the PVA/CS film demonstrates the excellent biocompatibility and low immunogenicity of the prepared e-skin (figs. S11 and S12). Figure 2B suggests a notable improvement in PPPA conductivity with higher aspect ratio AgNWs, reaching 12,000 S cm^{-1} at a ratio of 1:1.2. Comparison with PEDOT:PSS-based conductive materials modified by various approaches highlights the optimal conductivity achieved through this specific preparation method (table S1). However, further increasing the ratio is limited, as it heightens risk to cracking during fabrication process (fig. S13). In addition, the adhesiveness of the PPPA material ensures reliable electrical signal transmission with biological tissue (fig. S14A). On the other hand, mechanical deformations, such as stretching or bending, may change the electrical performance of the conductive network (fig. S14, B and C), while temperature and humidity also influence PPPA conductivity as environmental variables (fig. S15). A mere 15.51% increase in resistance is observed up to 20,000 bending cycles, indicating good reliability. Figure 2C illustrates a substantial decrease in the e-skin's contact impedance on the human body compared to the commercial Ag/AgCl gel electrode, reaching a minimum of only 35% of the gel electrode's impedance (see fig. S16 for test method). Compared with the reported PEDOT:PSS-based electrodes, the normalized contact impedance between PPPA and skin also reaches a very advanced level in this field (table S2).

The structure design of the HESS with a total weight of 105 g are depicted in fig. S17, where a composite TENG is designed to provide stable and highly controllable probing current. In this composite TENG, the output charge from the dc TENG is not only transferred for independent output to auxiliary diagnosis and integration with other medical devices but also transmitted to the ac TENG to amplify and stabilize the final output current (see Materials and Methods for manufacturing procedures). Figure S18 illustrates the detailed structure of this composite TENG system, where the challenges of prolonged response times, poor stability, and low interference resistance of traditional ac TENG can be solved by the charge injection form dc TENG into the ac component (see fig. S19 and note S2 for the detailed principle of composite TENG). This study proposes a dynamic balance strategy for the HESS to quantitatively optimize its electrical characteristics (see fig. S20 for details of dynamic balance strategy). This strategy, consisting of hardware design and operational adjustments, also exhibits substantial potential for all the other TENGs devices. First, a liquid medium, perfluorotri-*N*-butylamine, with a relative dielectric constant exceeding 40, replaces the air medium of TENG to eliminate the influence of parasitic capacitance (fig. S21; see note S3 for implementation method). After integrating the liquid medium, the root mean square (RMS) ripple of the dc TENG remarkably decreases (see note S4 for RMS ripple and ripple coefficient), effectively enhancing the source's filtering capability (fig. S21). Figure 2D illustrates the correction of operational imbalance of HESS, playing a pivotal role in minimizing ripple. Reducing operational imbalance factor from 1.02 to 0.1% results in an 88.69% decline in RMS ripple of the output voltage (fig. S22; testing and calibration methods are details in note S5). Furthermore, the dielectrics and electrode area also impact the performance of the electrical signal (figs. S23 and S24). For easy integration, the angle of the dielectrics is determined as 40°, the electrode angle is set at 5°, and other components are optimized with respect to these

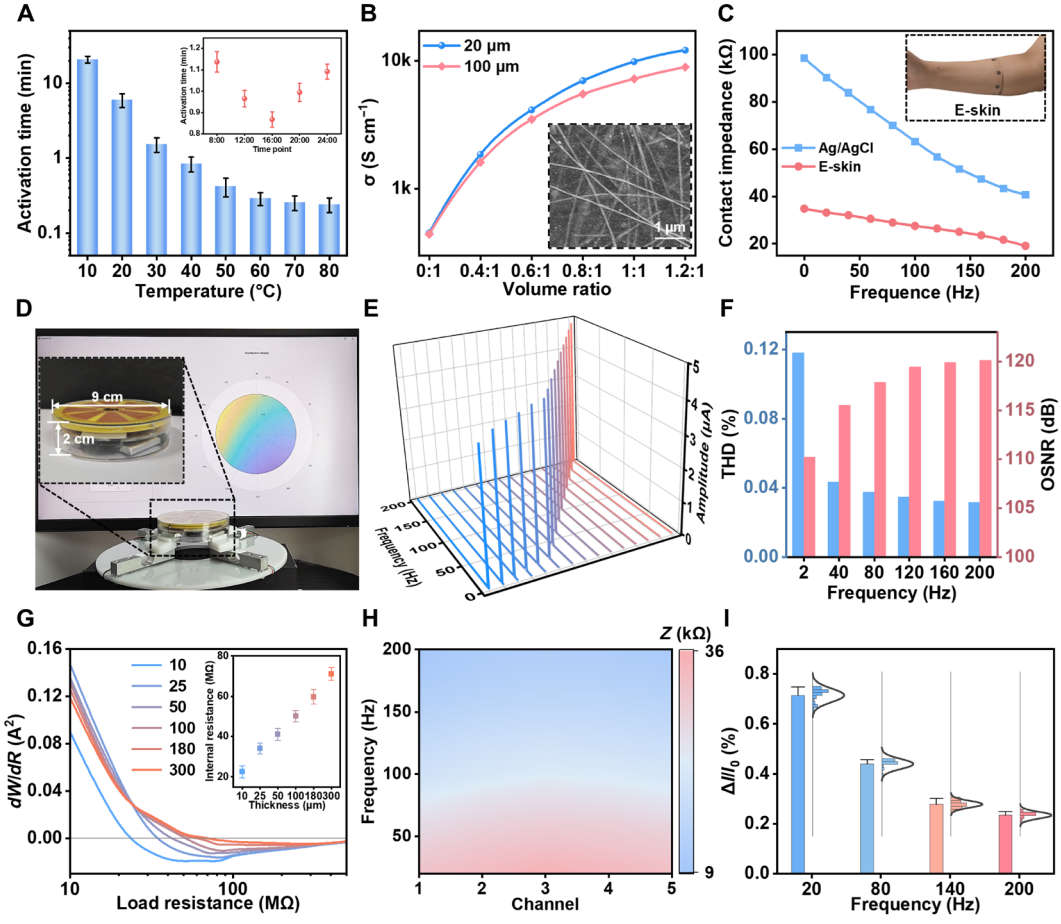

Fig. 2. Design scheme of e-skin and electrical parameter characterization of HESS. (**A**) The activation time of the adhesion layer at different temperatures. Inset: Activation time of the adhesion layer placed on human skin at different time points. (**B**) The electrical conductivity (σ) of the PPPA as a function of AgNW solution concentration and the length of AgNWs. The inset illustrates scanning electron microscopy images of the PPPA. (**C**) Comparison of the contact impedance between the e-skin and commercial AgCl/Ag electrode. (**D**) Instrumentation photos used for measuring and calibrating the operational imbalance of the HESS. The enlarged image displays physical photographs of the HESS. (**E**) Full spectrum of the current output from the HESS, ranging from 2 to 200 Hz with amplitudes between 4 and 5 μA. (**F**) Frequency response characteristics of the THD and OSNR of the ac signal. (**G**) The derivative curve obtained from the power curve of HESS, whose intersections with 0 correspond to the output resistance. The inset depicts the output resistance corresponding to different thicknesses of polytetrafluoroethylene (PTFE). (**H**) Human impedance (*Z*) distribution measured with the TIT principle. (**I**) The change in current amplitude of the HESS when loaded onto the human body at different operating frequencies. Each set of results is based on 100 data points. kΩ, kilohm; MΩ, megohm.

parameters. At the motion frequency of 50 Hz, the dc output of TENG achieves a high nominal voltage of 13 kV and a low current of 4.3 μA, with a ripple coefficient as minimal as 0.63%, while maintaining a ripple coefficient below 5% across the bandwidth (figs. S25 and S26). Comparing with a commercial high-voltage dc power supply, the ripple coefficient in this dc TENG at the same nominal voltage is only 57% (fig. S27).

On the basis of the charge injection driven by the high reverse resistance between dc and ac TENGs (fig. S28; see note S6 for test method), the short-circuit charge is increased by 148%, effectively addressing the slow startup issue associated with the absence of charge injection and remarkably enhancing signal quality (fig. S29). Through structural design and the implementation of a flexible contact strategy using rabbit fur and polytetrafluoroethylene (PTFE) as dielectrics, the risk of signal interruption due to surface wear in the rotating TENG is mitigated (fig. S30). The amplitude spectrum of the current signal indicates that the current intensity remains within 4 to 5 μA, exhibiting the weak frequency dependence particularly in the 20- to 200-Hz range (Fig. 2E), while, at higher frequencies, the current amplitude demonstrates a frequency-independent response due to reaching saturation (fig. S31). The results from Fig. 2F demonstrate that the overall THD of ac signal is below 1.2%, with a minimum of 0.03%, indicating a negligible impact of non-fundamental frequency components. In addition, the signal noise remains at an extremely low level, with an output signal-to-noise ratio (OSNR) exceeding 110 dB and reaching a peak of 120 dB (Fig. 2F) (see fig. S32 and note S4 for calculation details). When the installation position of the HESS is altered, the changes in the output signal are minimal, with the OSNR declining by only 2.44%, which is sufficient to ensure the normal functioning of the imaging capabilities of the TIT system (fig. S33).

The internal resistance of the current source is a key parameter related to the imaging quality. The composite TENG effectively addresses the fundamental challenge in circuit-based EIT systems—the

frequency response issue of the internal resistance in circuit-based current sources (*53*–*56*)—leading to a notable improvement in signal quality (fig. S34 and note S7). The modulation of the output resistance is implemented by controlling the thickness of PTFE with a positive correlation (Fig. 2G). Considering measurements of human body impedance (Fig. 2H; see fig. S35 and note S8 for test method), the internal resistance of the AC-TENG is constrained to a minimum of 50 megohms (thickness, 50 μm) within the frequency bandwidth (Fig. 2G and fig. S36). Consequently, when connected to the human body, the HESS exhibits a minimum output current variation rate of only 0.02% (Fig. 2I). The operational stability, noise, temperature, and vibration performance of the HESS are further examined to validate its long-term reliability as a component in the TIT device (fig. S37). Furthermore, the characteristics of the composite TENG and circuit-based current sources are compared (table S3), highlighting the advantages of using the composite TENG as a current source (see fig. S38 and note S9).

The microcontroller, featuring 64 data acquisition channels, is compactly designed at 5 cm by 5 cm and 34 g (fig. S39). To address the mismatch issues between electrostatic signals and electronic circuits, a state-adaptive resistance scheme is proposed (see note S10 for details). The collected time-domain signals are sent to the host computer via Zigbee for data processing (refer to note S11 for processing scheme). The time-frequency comparison of the voltage measured from the different instruments exhibits the reliability of the microcontroller measurements (fig. S40). For the image reconstruction of conductivity, the one-step Gauss-Newton (OGN) method is selected as the underlying framework, and a Gaussian high-pass filter is introduced as a regularization operator to enforce a unique estimation of the conductivity distribution based on boundary voltage. The final expression of the combined solving equation can be represented as

$$\Delta\vartheta = \left(\boldsymbol{J}^T\boldsymbol{C}^T\boldsymbol{C}\boldsymbol{J} + \lambda\boldsymbol{F}^T\boldsymbol{F}\boldsymbol{F}^T\boldsymbol{F}\right)^{-1}\boldsymbol{J}^T\boldsymbol{C}^T\boldsymbol{C}\boldsymbol{V}$$

where $\Delta\vartheta$ represents the conductivity change between two time points; $\boldsymbol{J}$ and $\boldsymbol{F}$ are the Jacobian matrix and filter matrix, respectively; $\boldsymbol{C}$ is the covariance matrix of the measured voltage values; λ is the regularization parameter; and V is the measured voltage change on the electrodes at the boundary (see note S12 for the derivation process). To mitigate characteristic features such as blurring, artifacts, and inaccurate phantom boundaries in image reconstruction from underlying algorithms, a six divine fires (SDF) algorithm is proposed and combined with a OGN algorithm, resulting in the construction of the SDF-OGN algorithm (see fig. S41 and note S13 for algorithm flowchart and details). In comparison to OGN method, the simulated images reconstructed by the SDF-OGN algorithm exhibit visually clearer shape boundaries while effectively suppressing artifacts (fig. S42A). This enhancement is further evidenced by the notable improvement in the quantitative metrics [RMS error (RMSE), structure similarity index measure (SSIM), peak signal-to-noise ratio (PSNR), and image correlation coefficient (ICC)] of the images reconstructed using the SDF-OGN method (table S4; see note S13 and fig. S42B for data training and validation). Furthermore, the comparison of the SDF-OGN algorithm's imaging results with those from reported linear approximation–based differential imaging algorithms demonstrates its superiority across all evaluation metrics, highlighting its critical contribution to the advanced capabilities of TIT devices (see table S5).

The tank model, with deionized water as the homogeneous medium and eight evenly spaced electrodes along the circumference, is applied for evaluating imaging quality and detection limits of this TIT system (Fig. 3A). Channel consistency in the open field is shown in fig. S43A, where each set of 40 date points forms eight stable U-shaped curves. Because of the superior data stability after processing (see fig. S43B for processing flow), frequency slice wavelet transform emerges as the preferred data preprocessing choice for image reconstruction (fig. S43C). The kernel density distribution of the relative SD (R_{SD}) shows that, in 10,000 repeated experiments, differences in R_{SD} among channels are generally centered around 0.09 to 0.1%, exhibiting excellent repeatability (fig. S43D; see note S14 for calculation detail). The system signal-to-noise ratio (SSNR), serving as a fundamental performance metric for evaluating the TIT system, is influenced by contact impedance (note S14). In the tank model, TIT with copper electrodes averages 104.6-dB SSNR, while PPPA electrodes also yield 102 dB (Fig. 3B).

In this study, all a priori information is inverted through the measured values to deal with poor adaptability and high error rate when directly measuring such information (see fig. S44 and note S15 for implementation steps). Figure 3 (C and D) and fig. S45 (A and B) present the image reconstruction results for different current injection frequencies in the tank model, confirming the reliability of target imaging through the distribution of ICC (Fig. 3E). For single-target imaging, in terms of actual perceptual effects, imaging performance reaches its optimum at 50 Hz (fig. S45C). In addition, the amplitude response with a distribution range close to 1 illustrates robust image reconstruction (fig. S45D and note S14). Figure 3F indicates that, under 200 repetitions, the system's average imaging accuracy can reach 98.18% (see note S14 for computational details), while the system exhibits a maximum achievable temporal resolution of 0.8 fps (Fig. 3G). In 200 experiments, the position error and RMSE distribution of the reconstructed image and the original image reach 0.147 and 0.012, respectively (Fig. 3H and note S14). However, compared to single-target imaging, both SSIM and PSNR are reduced in multi-target imaging (fig. S45E), and a decrease in excitation current further leads to a continuous decline in the SSNR and imaging quality (fig. S45F). Figure S46 shows that the minimum detection limit of the TIT system at the center position is effective for objects with a diameter of 1 mm, thereby defining the highest achievable spatial resolution of the TIT system at 1 mm/50 mm. Further mapping the spatial resolution onto conductivity, it can be deduced that the detection limit of the TIT system for cross-sectional conductivity variations is 0.0075 (see note S16 for calculation method). Therefore, in the dynamic imaging process of the tank model, the TIT system exhibits excellent robustness and operational stability (movie S1). In addition, the three-dimensional (3D) imaging with the TIT system is also contemplated. In contrast to traditional 3D tomographic scanning methods with multiple electrode layers, TIT prioritizes target objects, overcoming axial size limitations and reducing circuit complexity. Compared with the actual target, the volumetric error of the reconstructed target is only 5.26% (fig. S47; see note S17 for 3D reconstruction process).

By applying the TIT system to biological tissue measurements, the injected current frequency is controlled to be above 100 Hz (*57*–*59*). Relying on the inherent low current characteristics of HESS, the TIT system demonstrates a great advantage compared to other systems (table S6). The current density injected into the human body is only 79.58 to 99.47 mA m^{-2}, notably below the safety current thresholds

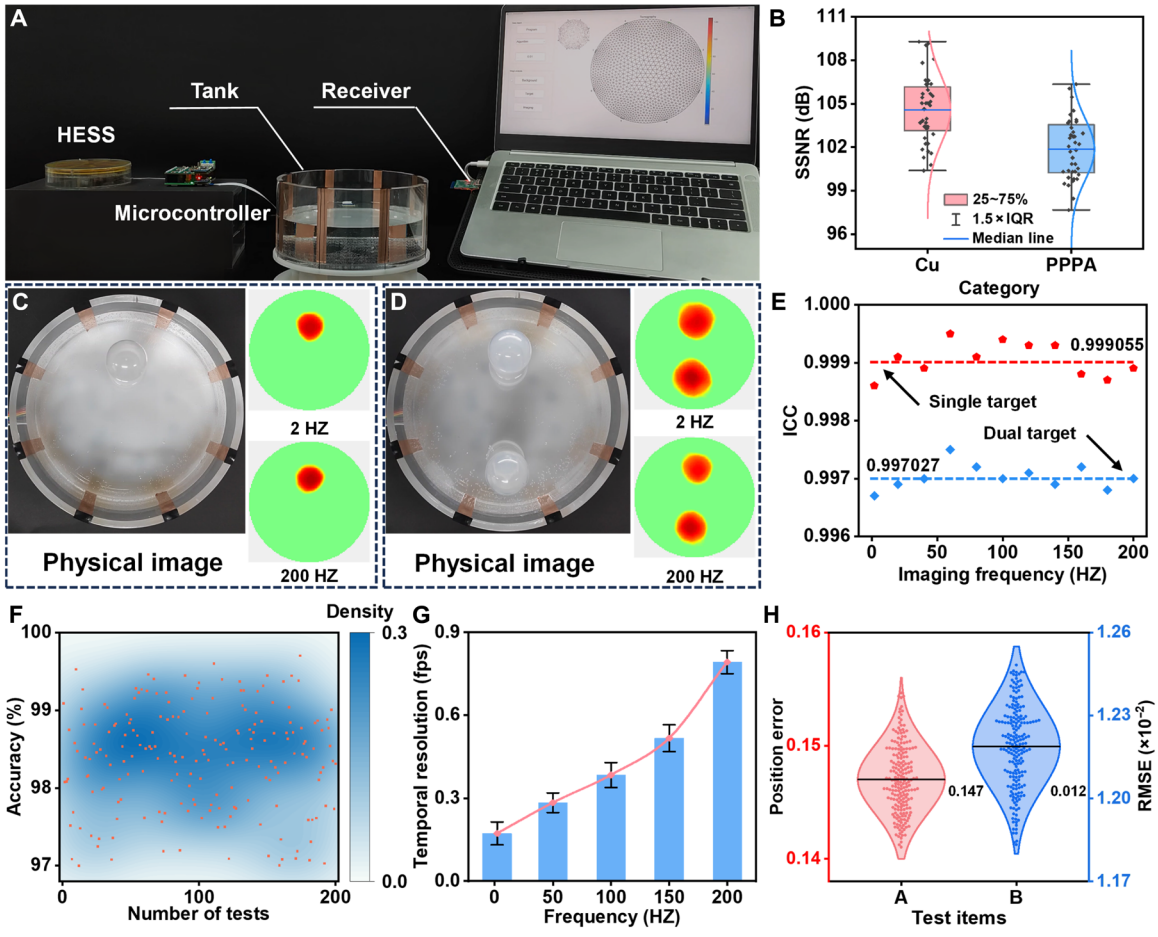

Fig. 3. Image reconstruction of targets in water tanks and evaluation of imaging results. (**A**) Photograph of the tank model. (**B**) SSNR exhibited by the TIT system with different electrode configurations with each test repeated 200 times. IQR, interquartile range. (**C** and **D**) The reconstructed images of single and multiple targets in the water tank using the TIT system, including results obtained with two injection currents of 2 and 200 Hz. In the test, the homogeneous polypropylene rod is selected as the detection target. (**E**) The ICC comparison for the reconstructed images of single-target and dual-target scenarios at different current injection frequencies. (**F**) Kernel density map of the imaging accuracy demonstrated by the TIT system, with 200 test trials. (**G**) Temporal resolution of the TIT device in response to frequency. (**H**) Evaluation of target position errors and RMSE in 200 tests.

stipulated by the IEC 60601 and GB 9706 standards for medical devices. For internal tissues of human body, the cellular types and the distribution of extracellular fluid substantially influence the electrical conductivity of biological tissues. This is manifested in the tissue-specific conductivity, such as fat (0.021 to 0.033 S m^{-1}), blood (0.52 to 0.83 S m^{-1}), and cerebrospinal fluid (1.79 to 1.81 S m^{-1}) (*60*, *61*), as well as the differential expression of tissue conductivity under various physiological states, exemplified by approximately a 10% change of conductivity during muscle transition from the steady state to contraction (*58*, *59*). These conductivity variations at the measured cross section can be fed back to the TIT system through boundary voltage, subsequently reconstructing the physiological state changes. As shown in fig. S48, the imaging results of ex vivo porcine tissue demonstrate the feasibility of the TIT device for identifying different biological tissue (muscle and fat).

In this case, TIT system can be configured on the human body and used to reconstruct soft tissue images inside forearm (fig. S49; see Materials and Methods section for human testing procedures). Figure S50A illustrates the electrode arrangement and MRI image of reference action. When the hand changes from a clenched fist to an extended index finger [Fig. 4A (i)], MRI shows marked muscle changes in the abductor pollicis longus and extensor indicis muscles, with small morphological alterations also in other tissues [Fig. 4A (ii)]. This phenomenon is also reflected in TIT images, where the red indicates a decrease in tissue conductivity, corresponding to the muscle contraction observed in the magnetic resonance imaging. Conversely, the blue regions imply an increase in conductivity, potentially attributed to muscle relaxation or tissue displacement [Fig. 4A (iii)]. The MRI and TIT systems reflect consistent locations of major muscle contractions, while the morphological and displacement changes of the radius and tibia, which are nearly negligible during the motion, are not captured in the reconstructed images.

The numerical statistics provide insights for further analyzing the contribution of tissues to motion, as well as for image recognition. The regional statistics of TIT images indicates that the maximum variation in the sum of pixels reaches −27.82 [Fig. 4A (iv)], corresponding to the region of maximum muscle contraction (see fig. S50B and note S18 for image segmentation methods). As the

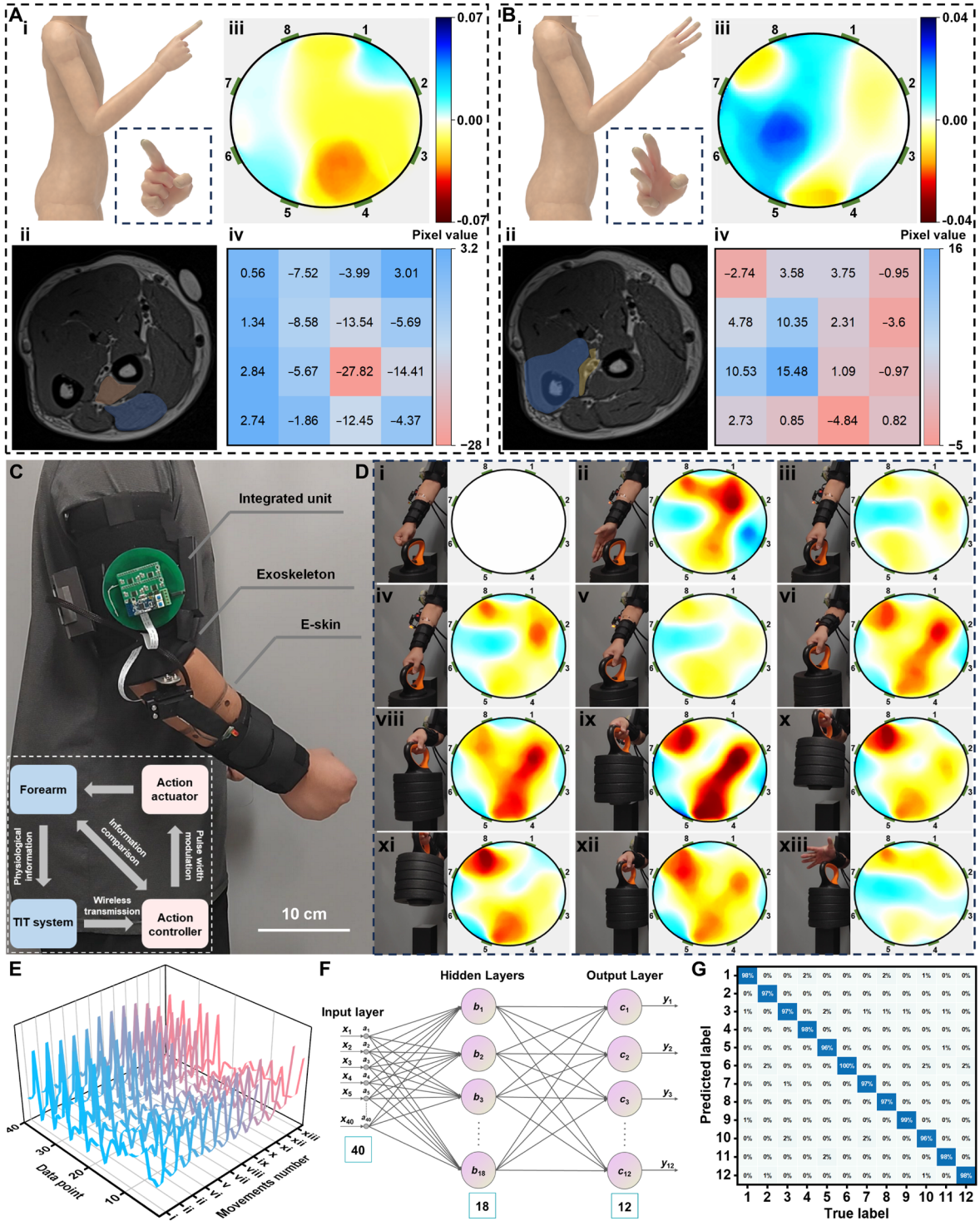

Fig. 4. Image reconstruction of upper limb movements by the TIT system and integration of the TIT system with medical-assistive exoskeleton. (**A**) The evaluation results of the TIT system for extending the index finger. (i) Schematic diagram of movement. (ii) MRI result, with color blocks indicating regions where marked changes occur. (iii) The reconstructed images of the TIT system. (iv) Regional change statistics of the reconstructed images. (**B**) The changes in the internal tissue when the simultaneous extension of the index, middle, and ring fingers. (i) Schematic diagram of movement. (ii) MRI picture. (iii) Reconstructed image. (iv) Regional change statistics. (**C**) Physical photograph of the integrated exoskeleton, where the integrated unit is the integration of the HESS and microcontroller. Inset: System framework and logical control description of the integrated exoskeleton. (**D**) The 12 motions (i to xiii) involved in the weight lifting experiment along with their reconstructed images. (**E**) The boundary data for 12 distinct motions. (**F**) Schematic diagram of the GA-BP model. (**G**) Classification results of the GA-BP model on the motion datasets.

extension of the index finger, middle finger, and ring finger [Fig. 4B (i)], the prominent changes appear in the flexor digitorum profundus muscle and adjacent vascular tissues [Fig. 4B (ii)]. This is manifested in the TIT image as an increase in the conductivity of the corresponding region, indicating relaxation of the associated tissues in this area [Fig. 4B (iii)]. Figure 4B (iv) quantifies the variations in each region and locates the region with the most substantial changes. Figure S50C further characterizes MRI and reconstructed images when all fingers are fully extended. The dynamic imaging process of hand movements validates the feasibility of the TIT system in providing rapid feedback on internal soft tissue changes (movie S2). The reconstructed images of internal physiological changes during upper limb movements by the TIT system, depicted in fig. S51 (A and B), demonstrate the system's detection sensitivity to forearm movements as low as 3° (fig. S51C). When hand movement is further incorporated into upper limb motion, the reconstructed images are depicted in fig. S51B. The boundary voltages for the above five movements are illustrated in fig. S51D. Two hundred such sets are continuously collected for each movement, which is randomly divided into two groups (training, 160; and testing, 40). Importing testing data into the particle swarm optimization and support vector machine model results in the classification average accuracy of 94.4% (fig. S51E; see table S7 and note S19 for optimization details). Furthermore, the TIT system also demonstrates the capability to detect multiple various actions, including forearm rotation and extension (fig. S52), as well as strong environmental adaptability, ensuring reliable imaging even when the human body is sweating (fig. S53).

Therefore, compared to the typical EIT systems (as shown in table S6), the TIT device offers several distinct advantages. The TIT device operates at substantially lower frequencies and excitation currents, which is particularly beneficial for long-term monitoring. The ability to maintain high imaging quality with such low excitation current is a notable achievement, addressing a common challenge in traditional EIT systems. What is more, the TIT system achieves a higher signal-to-noise ratio (SNR), which directly enhances the imaging quality. This improvement is crucial given the low excitation current, as maintaining a high SNR under these conditions is typically difficult. The system's high-quality multimodal signals not only enable the effective diagnosis of internal microlesions but also support other functionalities in wearable devices. The TIT device features a self-designed e-skin that effectively reduces the contact impedance between the electrodes and the skin. This method minimizes interface effects and prevents electrode drying issues during prolonged monitoring sessions. Last, the TIT system is engineered for reliable long-term stability. Its performance not only meets but often surpasses that of conventional circuit-based systems, ensuring consistent and dependable operation over extended periods. In addition, the comparison between the TIT system and typical wearable ultrasound systems is further summarized in table S8.

Then, the TIT device is integrated with a medical-assistive exoskeleton to demonstrate its applicability (fig. S54; see note S20 for the design scheme). The exoskeleton equipped with the TIT device is shown in Fig. 4C, with e-skin attached to the forearm testing area. The HESS and microcontroller, after integration, are mounted on the exoskeleton through a quick-detach structure. The inset in Fig. 4C illustrates the system framework and control logic of the exoskeleton integrated with the TIT device. The user of the exoskeleton, such as myasthenia patients, intends to perform upper limb movements, and the related changes in muscles shape as well as the triggered chain reaction in nearby tissues can all be identified by the TIT system. Consequently, the established connection between the TIT image and the wearer's movement intention can guide the medical-assistive exoskeleton to produce auxiliary force, which can help the myasthenia patients to accomplish different movements. The weightlifting experiment is conducted to assess the performance of the integrated exoskeleton, with a load of 10.5 kg. The experiment includes 12 movements, with their reconstructed images shown in Fig. 4D, where the first movement is the reference action [Fig. 4D (i and ii)]. When detecting the hand grip, the exoskeleton remains dormant, indicating that the tissue changes do not provide sufficient information to predict the next arm action [Fig. 4D (iii)]. However, when the conductivity of power-providing muscle further decreases, although the weight is not actually lifted, the human intention of movement mapped through soft tissue changes is captured by the TIT system [Fig. 4D (iv)]. This information causes the exoskeleton to transition into the active state, leading to the notable relaxation of relevant tissues [Fig. 4D (v)]. Throughout the subsequent exoskeleton-assisted upper limb movements until completion, the TIT system continuously transmits internal tissue information back to the controller to assess the user's motion intention [Fig. 4D(vi to xii)]. The data involving 12 movements is illustrated in Fig. 4E, and the movement dataset (80% allocated to the training set) subsequently incorporated into the genetic algorithm–optimized back-propagation (GA-BP) neural network. The GA-BP network includes three layers with 40 neurons in the input layer, 18 neurons in the hidden layer, and 12 neurons in the output layer (Fig. 4F). The average accuracy of the GA-BP model trained on 12 movements is 97.58%, demonstrating high recognition accuracy and rapid convergence speed (Fig. 4G and fig. S55; see note S21 and table S9 for optimization parameters). Leveraging the intelligent enhancement based on the GA-BP model, the integrated exoskeleton reliably provides force support aligned with the wearer's intentions (movie S3).

In contrast to conventional wearable sensors, the TIT system not only can discern muscle movements but also can detect the deep-seated pathological change of soft tissues. A 64-year-old female patient with forearm lipoma is invited for pathological tissue detection. Lipoma is primarily composed of dense adipose tissue [Fig. 5A (i and ii)], resulting in the electrical conductivity substantially lower than that of other soft tissues (*60*). The reconstructed images demonstrate the feasibility of TIT system in evaluating the presence, location, and orientation of lipomas [Fig. 5A (iii)]. The lesion area in the reconstructed images of TIT (depicted in black) is slightly larger than that observed by MRI, which is attributed to the lower threshold value selected for enhancing the compatibility of the TIT system in lesion detection. In addition, the consecutive comparison is conducted on the MRI and TIT images of the forearms in both healthy volunteers and patients to evaluate the image differences at different locations (movie S4). Figure 5B (i to vi) illustrates cross-sectional images reconstructed by the TIT system at various positions, with the starting point located 13 cm below the elbow joint [Fig. 5B (i)] and the endpoint at the wrist joint [Fig. 5B (vi)]. Figure 5C (i) illustrates the 3D model of the lipoma constructed from the images in Fig. 5B, with the volume difference of only 5% compared to the 3D model established by MRI (fig. S56). As depicted by the integrated forearm model containing lipoma and its cross-sectional images, the model exhibits high fidelity,

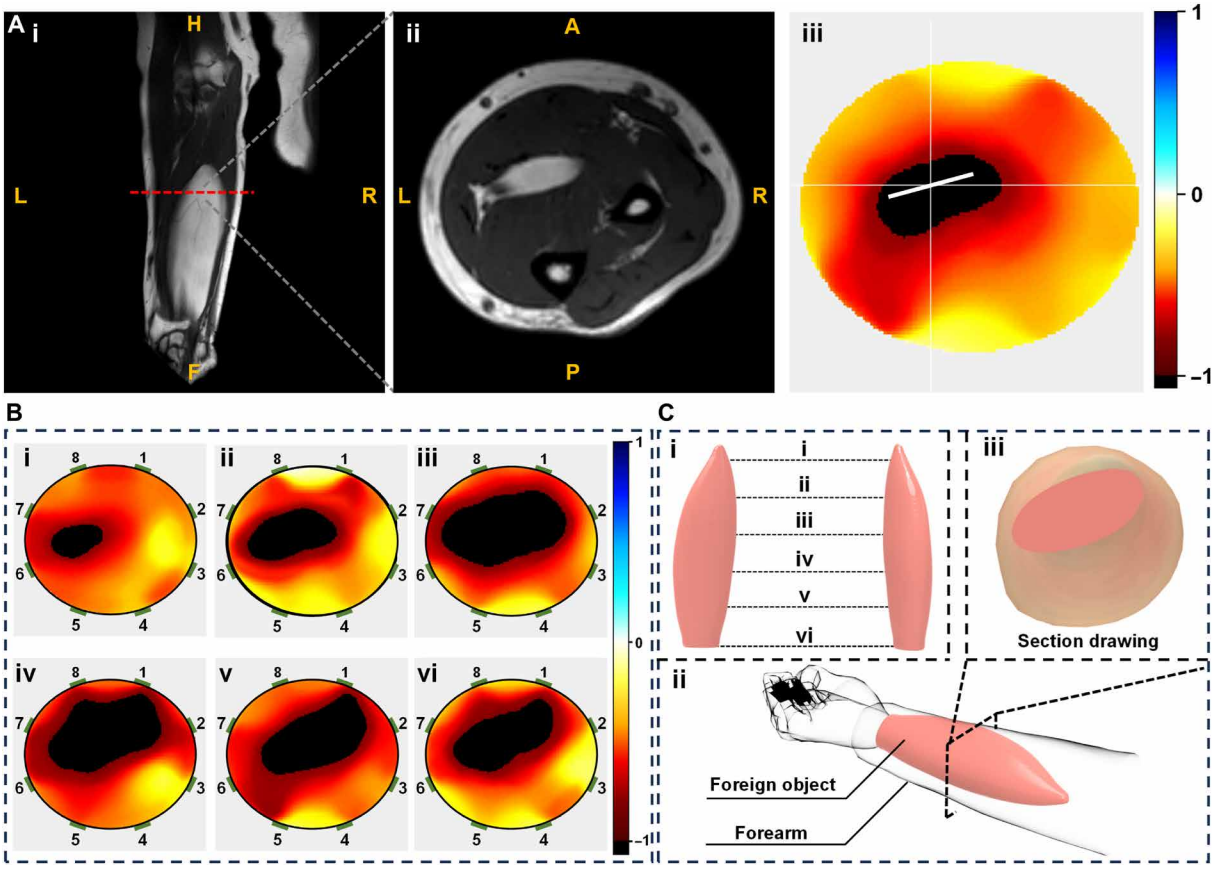

Fig. 5. Reconstruction of images for forearm lipomas by the TIT system and evaluation of imaging results. (**A**) The MRI images of the patient, along with the images reconstructed by the TIT system. (i) Coronal MRI graph. (ii) Corresponding MRI cross-sectional images. (iii) Reconstructed TIT images, which reveals information such as the presence, size, and location of lipomas. (**B**) The images at different positions (i to vi), with a longitudinal spacing of 4.5 cm. (**C**) The 3D model constructed from sectional images. (i) Reconstructed 3D model of the lipoma, where (i) to (iv) correspond to six sectional images. (ii) Localization and morphology of the lipoma within the forearm model. (iii) Cross-sectional images of the forearm model.

meeting the visualization requirements of pathological tissues [Fig. 5C (ii and iii)].

Besides direct detection reserved for pathological tissues, the TIT system also demonstrates efficacy in indirectly discerning subtle injuries by identifying changes of interstitial fluid, owing to the high conductivity of interstitial fluid (usually ≥1 S m^{-1}) readily detectable by the TIT system (*61, 62*). A 15-year-old adolescent with closed injury is invited to participate as a test subject [Fig. 6A (i)]. The skin does not manifest visible symptoms, with the patient reporting only mild discomfort. In the obtained results [Fig. 6A (ii to iv)], Fig. 6A (iii) exhibits distinctive features, characterized by elevated conductivity (depicted in blue). In this frame, the maximum change in the target region is 17.03 (Fig. 6B). However, because of the smaller size of the detection target, it is necessary to incorporate absolute capacitance for further auxiliary discrimination to reduce the probability of misjudgment. Unlike the differential mode of tomographic imaging, the absolute capacitance relies on the injected current by dc TENG and avoids the impact of prior information error (fig. S57; see note S22 for details). The composite TENG can independently output high-quality dc signals, which facilitates the implementation of this strategy. Because of differences in the physiological tissues covered by each electrode pair, the capacitance values from the four channels exhibit distinctive features (movie S5), and these values are also influenced by human motion (fig. S58). According to absolute capacitance obtained from standard upper limb movements (fig. S59), the relative variation rate in channel (iii) (2.37%) is substantially lower compared to that in the other three channels, which implies the presence of substances, causing a decrease in capacitance (Fig. 6C). X-ray imaging confirmed TIT system test results, with cracks on the radius (length, 16 mm), implying that fractures causing tissue exudation and cysts may be the primary factors, leading to the increase in conductivity and corresponding decrease in capacitance (Fig. 6D). Adjacent positions are measured starting from the location of Fig. 6A (iii) to determine the axial range of abnormal area. The results revealed that the length of the abnormal tissue region in the axial direction reached 20 mm, slightly exceeding the fracture area range provided by x-ray imaging (Fig. 6E).

DISCUSSION

This study introduces a TIT system for imaging human soft tissues, which relies on the analysis of impedance information of different soft tissues and movable biological fluids inside human body.

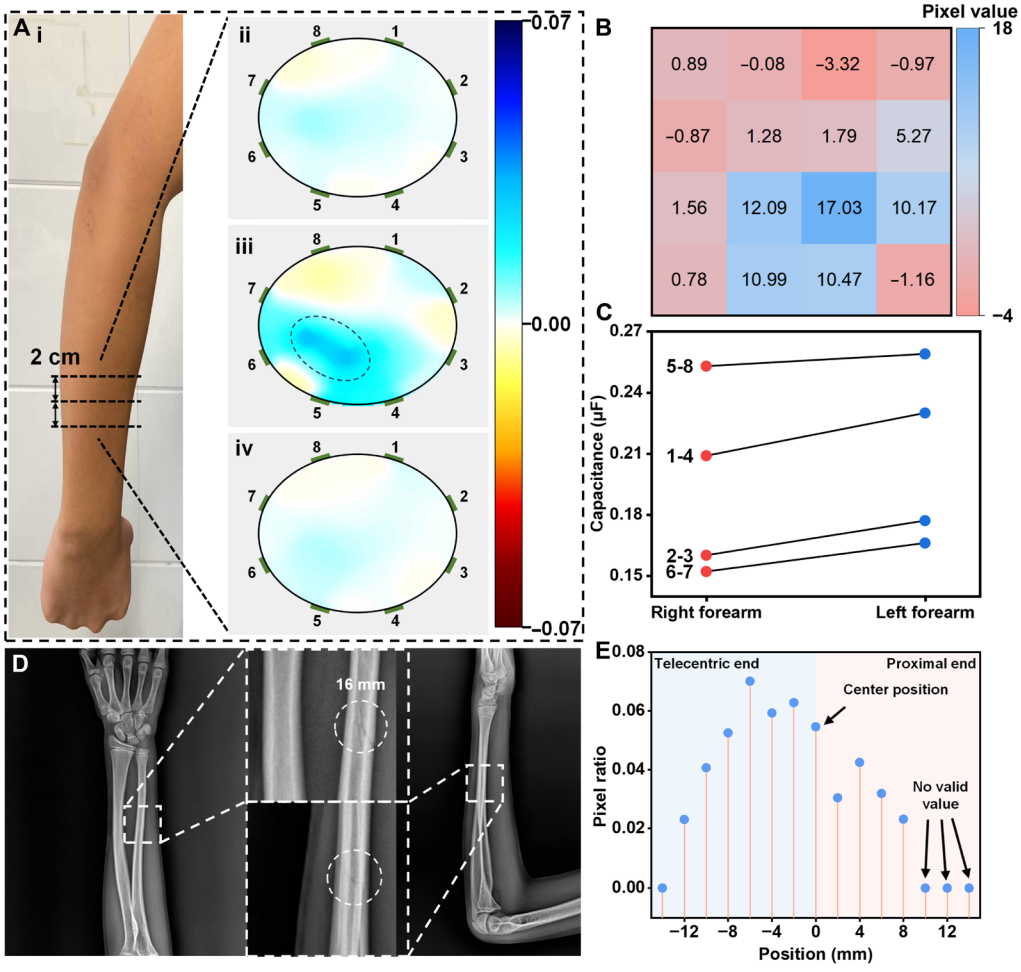

Fig. 6. The identification and reconstruction of pathological tissues caused by fractures using the TIT system. (**A**) The schematic diagram of TIT forearm testing (i) and the images at the respective locations (ii and iii). (**B**) Regional variation statistics of the image in A(iii). (**C**) Comparison of capacitance values at the testing positions on the left and right forearms of the patient, where 1-4, 2-3, 5-8, and 6-7 are the four electrode pairs (i to iv). (**D**) X-ray imaging of the patient's left radius and ulna in the anteroposterior and lateral views. (**E**) Axial extent of the increase region in conductivity measured by the TIT system.

Combined with a tailored microcontroller and a machine learning–optimized reconstruction algorithm, the calculated impedance distribution within the targeted cross section can be used to achieve noninvasive imaging of biological tissues and identifying abnormal tissues. The high-quality and biocompatible current signal source is the core elements for the TIT system. A composite TENG with a specially designed dc-ac–amplifying strategy is proposed as the sweeping signal source, where its current amplitude and output impedance exhibit frequency-independent response characteristics after reaching operational equilibrium. The signal source including TENG, motor, and controlling circuits is integrated into a module with the size of 9 cm by 9 cm by 2 cm. Last, this HESS under the drive of the composite TENG obtains a current intensity of 4 to 5 μA and exhibits the minimal THD of only 0.03% and a peak OSNR of up to 120 dB. These THD and noise parameters have never been realized by the electrostatic power source based on TENG device. The current density injected into the human body is only 79.58 to 99.47 mA m^{-2} with only a 0.02% variation in output current, substantially below the safety current thresholds stipulated by the IEC 60601 and GB 9706 standards for medical devices. If commercially available ac current sources want to obtain the similar level of high-quality and low-intensity signals, then it requires a much more complex system. Hence, the HESS based on the composite TENG is so far the best option for this wearable impedance tomography system. The TIT system demonstrated an average SSNR of 102 dB in practical testing, achieving an unparalleled level in wearable impedance tomography systems. Coupled with the SFD-OGN algorithm developed in this work, the TIT system achieves a maximum measured spatial resolution of 1 mm/50 mm, and high-fidelity imaging results in an imaging accuracy of 98.18% and an ICC of 0.9995. To our best acknowledgement, the tomography of human limbs' soft tissues has never been reported before. In this case, the TIT system can distinguish the lifting motion of the forearm around the elbow joint, with the minimum detection angle as low as 3°. The integration experiments of TIT system and medical-assistive exoskeleton indicate that the TIT device efficiently identifies users' motion intentions with the average accuracy of 95.4%, guiding the exoskeleton to assist limb movements. In addition to muscle movements, this TIT device can also detect the deep-seated pathological change of soft tissues. The 3D modeling results generated from the scanned impedance information

of a lipomas on the forearm using TIT system shows a volume difference of only 5% compared to MRI results. Combined with the absolute capacitance analysis, the TIT system can briefly complete the microfracture determination for a closed injury on the forearm, a task that previous wearable EIT devices could not accomplish under similar conditions due to the minute size of the lesions. This TIT system introduces a promising approach for wearable soft tissue imaging with superior compatibility and high integration, which can support various promising applications in human-machine interaction, exoskeleton-assisted therapy, outdoor medical care, and so on.

MATERIALS AND METHODS

Preparation steps of e-skin

The fabrication of PVS/CS solution

PVA powder (P13954, Aladdin) was dissolved in pure water at 60°C for 1 hour, followed by stirring at 100°C for 3 hours, to prepare a 10 wt % PVA solution. In addition, the CS (C804726, Macklin) powder was added in 1% acetic acid solution to prepare a 2% (w/v) CS solution. The PVA solution and CS solution were mixed in a 1:1 mass ratio with 5% glycerol (G116206, Aladdin). After stirring for 30 min, the mixture was allowed to stand for 1 hour to degas, resulting in a PVA/CS solution with a viscosity of 0.7 Pa·s.

Fabrication of PPPA conductive material

Glycerol (10 wt %) was added into the PEDOT:PSS solution (885, Xin Shuangjian Technology Co. Ltd.), and ultrasonic oscillation was applied for 60 min. Subsequently, the aqueous PU solution (F0415, Jitian chemical Co. Ltd.) was added to the mixed ink with a volume ratio of 1:2, and the secondary mixed ink was obtained after stirring for 10 min. In addition, the AgNW solution (L30, XFNano Technology Co. Ltd) was diluted with deionized water to three times its original volume and then incrementally added to the secondary mixed ink. The volume ratio of the two was treated as a variable in this process. Subsequently, the mixture was stirred at 70°C for 30 min to obtain PPPA.

Assembly of e-skin

The prepared PVA/CS solution was added onto a nonstick paper surface and evenly spread by a scraper. The liquid film was dried at 60°C for 1 hour to obtain an encapsulation layer (height, 5 μm). A suitable amount of silicon fluoride (207c, Zhongke Lingchuang Technology Co. Ltd) solution was rapidly sprayed onto the substrate surface with the spray gun, followed by drying at 60°C for 1 hour. The treated encapsulation layer was transferred onto a clean nonstick paper, with the unmodified side facing outward. The circuit template was placed on the surface of the encapsulation layer, and circuit printing was performed with prepared PPPA, followed by drying at 80°C for 15 min. Through the 3D print, the PVA/CS pattern was selectively coated onto the circuit to prepare a supporting layer, leaving the test electrodes and circuit interface uncovered. Test electrode height was extended with a pipette to ensure that it exceeded that of the supporting layer, resulting in an extended electrode height of ~5 μm. Furthermore, the electrodes were covered with a masking board, and a PVA/CS solution was applied on the supporting layer to construct an adhesive layer for skin attachment. The electrode masking board was removed from the prepared e-skin, and a layer of release paper is placed over the surface of the e-skin to isolate it from the air. The prepared e-skin can be stored in light-protected conditions or in a refrigerator if conditions permit.

Design and fabrication of the HESS

The HESS was designed and modeled using SolidWorks. The printed circuit board was designed with Altium Designer and fabricated through conventional methods, featuring a substrate thickness of 0.6 mm. The acrylic plate (1 mm) was shaped by the laser cutting machine. The brushless motor (TMOTOR P1804, diameter of 22.9 mm) serves as the power generator, with the driver (Raptor-5 G071) being appropriately matched to it. The encapsulation shell was produced by 3D printing technology, featuring an interference fit with the main body of the HESS.

Testing procedure on the forearm of the participants

Explanation related to human research participants

The human testing procedures involved in the experiment were conducted in accordance with the approved experimental protocol (A-2019027) by the Ethics Committee of the Beijing Institute of Nanoenergy and Nanosystems. Inclusion criteria for volunteers were defined as individuals aged 20 to 60 years, with a body weight ranging from 50 to 80 kg. Subjects may have the following with unhealthy limbs or related issues problems (cysts, tumors, and fractures). This experiment involved a total of 12 volunteers, including 10 healthy volunteers, one individual with forearm lipoma, and one individual with forearm fracture. All participants provided written informed consent. For the publication of identifiable images of research participants, it was confirmed that consent was obtained for publication.

Acquisition of data from healthy volunteers

Before to the initiation of testing, each subject's forearm was wiped with a medical alcohol swab. When detecting hand movements through the TIT system, participants were instructed to assume a standing position with a 75° angle between the forearm and upper arm. The e-skin was affixed at 10 cm from the elbow joint, while hand movements were performed as instructed. When conducting upper limb movements and exoskeleton testing, subjects wore the assistive exoskeleton as instructed, ensuring that the placement of the e-skin adhered to the same specifications as outlined in the above tests. Subsequently, participants executed the specified movements in accordance with the experimental instructions.

Collection of data from patients with forearm lipomas

The patient is 64 years old, weighs 70 kg, and has no history of other tumor-related illnesses. Considering the patient's physical condition, the testing was conducted with the patient in a seated position, where the patient was required to keep the forearm hanging naturally with the palm open. Other testing requirements remained consistent with the mentioned data acquisition process for healthy volunteers.

Collection of boundary voltage data in patients with fractures

Before the TIT test starts up, different areas of the forearm were pressed to observe the patient's pain regions, along with the nature and intensity of pain. Once the most pronounced painful area was identified, it was cleaned and subjected to testing. In addition, testing at positions extending proximally and distally from the identified location was conducted following the same requirements. The testing procedure for capacitance units in fracture patients followed the same steps as described above. However, it was conducted in a

seated position to minimize any potential shaking caused by prolonged standing.

Experiment measurement and characterization

The programmable electrostatic voltmeter (Model 6517, Keithley) and electrostatic voltmeter (Model 341B, Advanced Energy Industries) were used to measure the current and voltage of the HESS, respectively. Signal acquisition and recording were carried out by a signal acquisition card (Model USB-6356, National Instruments). The MRI system (Siemens Prisma 3.0T) was used to obtain physiological tissue images of volunteers. In addition, x-ray images of the patient with a fracture were captured using a digital x-ray imaging system (New Huangpu KD1800DR). An infrared camera (Model 225s, Fotric) was used for observing temperature variations involved in the experiment. The contact angle goniometer (Model CA100C, Innuo) was used for measuring the contact angle between liquid medium and dielectric materials. A source meter (Keithley 2450) with a four-point probe (HP-504, 4Probes Tech Ltd.) was used to characterize the surface conductivity of PPPA. A scanning electron microscope (SU8020, Hitachi) was used for the characterization of the surface morphology and layered structure of PPPA.

Statistics and reproducibility

All experiments were repeated at least three times. Data were analyzed as means ± SD. Nominal values ± RMSE were used for statistical assessment of dc output of HESS. Statistical analyses for multiple samples were conducted and presented through various graphical representations such as normal distribution plots, box plots, density plots, and violin plots. Relevant sample data points were directly visualized in the graphs. Data analysis and graphical representation were carried out using Origin 2023 and Excel.

Supplementary Materials

The PDF file includes:

Figs. S1 to S59
Notes S1 to S22
Tables S1 to S9
Legends for movies S1 to S5

Other Supplementary Material for this manuscript includes the following:

Movies S1 to S5

REFERENCES AND NOTES

1. H. Hu, H. Huang, M. Li, X. Gao, L. Yin, R. Qi, R. S. Wu, X. Chen, Y. Ma, K. Shi, C. Li, T. M. Maus, B. Huang, C. Lu, M. Lin, S. Zhou, Z. Lou, Y. Gu, Y. Chen, Y. Lei, X. Wang, R. Wang, W. Yue, X. Yang, Y. Bian, J. Mu, G. Park, S. Xiang, S. Cai, P. W. Corey, J. Wang, S. Xu, A wearable cardiac ultrasound imager. *Nature* **613**, 667–675 (2023).
2. C. Wang, X. Chen, L. Wang, M. Makihata, H.-C. Liu, T. Zhou, X. Zhao, Bioadhesive ultrasound for long-term continuous imaging of diverse organs. *Science* **377**, 517–523 (2022).
3. E. Boto, N. Holmes, J. Leggett, G. Roberts, V. Shah, S. S. Meyer, L. D. Muñoz, K. J. Mullinger, T. M. Tierney, S. Bestmann, G. R. Barnes, R. Bowtell, M. J. Brookes, Moving magnetoencephalography towards real-world applications with a wearable system. *Nature* **555**, 657–661 (2018).
4. M. Lin, H. Hu, S. Zhou, S. Xu, Soft wearable devices for deep-tissue sensing. *Nat. Rev. Mater.* **7**, 850–869 (2022).
5. J. Frahm, D. Voit, M. Uecker, Real-time magnetic resonance imaging: Radial gradient-echo sequences with nonlinear inverse reconstruction. *Invest. Radiol.* **54**, 757–766 (2019).
6. M. M. Lell, M. Kachelrieß, Recent and upcoming technological developments in computed tomography: High speed, low dose, deep learning, Multienergy. *Invest. Radiol.* **55**, 8–19 (2020).
7. N. Petruzzi, N. Shanthly, M. Thakur, Recent trends in soft-tissue infection imaging. *Semin. Nucl. Med.* **39**, 115–123 (2009).
8. W. Goth, J. Lesicko, M. S. Sacks, J. W. Tunnell, Optical-based analysis of soft tissue structures. *Annu. Rev. Biomed. Eng.* **18**, 357–385 (2016).
9. F. Feldchtein, V. Gelikonov, R. Iksanov, G. Gelikonov, R. Kuranov, A. Sergeev, N. Gladkova, M. Ourutina, D. Reitze, J. Warren, In vivo OCT imaging of hard and soft tissue of the oral cavity. *Opt. Express* **3**, 239–250 (1998).
10. Y. Baribeau, A. Sharkey, O. Chaudhary, S. Krumm, H. Fatima, F. Mahmood, R. Matyal, Handheld point-of-care ultrasound probes: The new generation of POCUS. *J. Cardiothorac. Vasc. Anesth.* **34**, 3139–3145 (2020).
11. Y. Fan, P. Wang, Y. Lu, R. Wang, L. Zhou, X. Zheng, X. Li, J. A. Piper, F. Zhang, Lifetime-engineered NIR-II nanoparticles unlock multiplexed in vivo imaging. *Nat. Nanotechnol.* **13**, 941–946 (2018).
12. J. Kim, A. S. Campbell, B. E.-F. de Ávila, J. Wang, Wearable biosensors for healthcare monitoring. *Nat. Biotechnol.* **37**, 389–406 (2019).
13. H. C. Ates, P. Q. Nguyen, L. Gonzalez-Macia, E. Morales-Narváez, F. Güder, J. J. Collins, C. Dincer, End-to-end design of wearable sensors. *Nat. Rev. Mater.* **7**, 887–907 (2022).
14. M. Bariya, H. Y. Y. Nyein, A. Javey, Wearable sweat sensors. *Nat. Electron.* **1**, 160–171 (2018).
15. J. Dunn, L. Kidzinski, R. Runge, D. Witt, J. L. Hicks, S. M. Schüssler-Fiorenza Rose, X. Li, A. Bahmani, S. L. Delp, T. Hastie, M. P. Snyder, Wearable sensors enable personalized predictions of clinical laboratory measurements. *Nat. Med.* **27**, 1105–1112 (2021).
16. W. Du, L. Zhang, E. Suh, D. Lin, C. Marcus, L. Ozkan, A. Ahuja, S. Fernandez, I. I. Shuvo, D. Sadat, W. Liu, F. Li, A. P. Chandrakasan, T. Ozmen, C. Dagdeviren, Conformable ultrasound breast patch for deep tissue scanning and imaging. *Sci. Adv.* **9**, eadh5325 (2023).
17. C. K. S. Park, T. Trumpour, A. Aziz, J. S. Bax, D. Tessier, L. Gardi, A. Fenster, Cost-effective, portable, patient-dedicated three-dimensional automated breast ultrasound for point-of-care breast cancer screening. *Sci. Rep.* **13**, 14390 (2023).
18. S. Shahrestani, G. Zada, T.-C. Chou, B. Toy, B. Yao, N. Garrett, N. Sanossian, A. Brunswick, K.-M. Shang, Y.-C. Tai, Noninvasive transcranial classification of stroke using a portable eddy current damping sensor. *Sci. Rep.* **11**, 10297 (2021).
19. G. Blumrosen, C. A. Gonzalez, B. Rubinsky, in *2009 Sixth International Workshop on Wearable and Implantable Body Sensor Networks* (IEEE, 2009), pp. 120–124.
20. J. Chen, G. Li, M. Chen, G. Jin, S. Zhao, Z. Bai, J. Yang, H. Liang, J. Xu, J. Sun, M. Qin, A noninvasive flexible conformal sensor for accurate real-time monitoring of local cerebral edema based on electromagnetic induction. *PeerJ* **8**, e10079 (2020).
21. T.-G. La, L. H. Le, Flexible and wearable ultrasound device for medical applications: A review on materials, structural designs, and current challenges. *Adv. Mater. Technol.* **7**, 2100798 (2022).
22. L. Zhang, W. Du, J.-H. Kim, C.-C. Yu, C. Dagdeviren, An emerging era: Conformable ultrasound electronics. *Adv. Mater.* **36**, e2307664 (2024).
23. M. Amjadi, K.-U. Kyung, I. Park, M. Sitti, Stretchable, skin-mountable, and wearable strain sensors and their potential applications: A review. *Adv. Funct. Mater.* **26**, 1678–1698 (2016).
24. S. Patel, H. Park, P. Bonato, L. Chan, M. Rodgers, A review of wearable sensors and systems with application in rehabilitation. *J. Neuroeng. Rehabil.* **9**, 21 (2012).
25. S. Ajami, F. Teimouri, Features and application of wearable biosensors in medical care. *J. Res. Med. Sci.* **20**, 1208–1215 (2015).
26. P. Metherall, D. C. Barber, R. H. Smallwood, B. H. Brown, Three-dimensional electrical impedance tomography. *Nature* **380**, 509–512 (1996).
27. E. Ravagli, S. Mastitskaya, N. Thompson, F. Iacoviello, P. R. Shearing, J. Perkins, A. V. Gourine, K. Aristovich, D. Holder, Imaging fascicular organization of rat sciatic nerves with fast neural electrical impedance tomography. *Nat. Commun.* **11**, 6241 (2020).
28. C. Ding, Y. Zhu, S. Zhang, Z. Zhao, Y. Gao, Z. Li, Bedside electrical impedance tomography to assist the management of pulmonary embolism: A case report. *Heliyon* **10**, e25159 (2024).
29. I. Frerichs, J. Hinz, P. Herrmann, G. Weisser, G. Hahn, T. Dudykevych, M. Quintel, G. Hellige, Detection of local lung air content by electrical impedance tomography compared with electron beam CT. *J. Appl. Physiol.* **93**, 660–666 (2002).
30. N. Goren, J. Avery, T. Dowrick, E. Mackle, A. Witkowska-Wrobel, D. Werring, D. Holder, Multi-frequency electrical impedance tomography and neuroimaging data in stroke patients. *Sci. Data* **5**, 180112 (2018).
31. S. Martin, C. T. M. Choi, A post-processing method for three-dimensional electrical impedance tomography. *Sci. Rep.* **7**, 7212 (2017).
32. Y. Li, N. Wang, L.-F. Fan, P.-F. Zhao, J.-H. Li, L. Huang, Z.-Y. Wang, Robust electrical impedance tomography for biological application: A mini review. *Heliyon* **9**, e15195 (2023).
33. A. McEwan, G. Cusick, D. S. Holder, A review of errors in multi-frequency EIT instrumentation. *Physiol. Meas.* **28**, S197–S215 (2007).
34. Z. Zong, Y. Wang, Z. Wei, A review of algorithms and hardware implementations in electrical impedance tomography (invited). *Prog. Electromagn. Res.* **169**, 59–71 (2020).
35. M. Bodenstein, M. David, K. Markstaller, Principles of electrical impedance tomography and its clinical application. *Crit. Care Med.* **37**, 713–724 (2009).

36. O. Gilad, L. Horesh, D. S. Holder, Design of electrodes and current limits for low frequency electrical impedance tomography of the brain. *Med. Biol. Eng. Comput.* **45**, 621–633 (2007).
37. D. Liebetanz, R. Koch, S. Mayenfels, F. König, W. Paulus, M. A. Nitsche, Safety limits of cathodal transcranial direct current stimulation in rats. *Clin. Neurophysiol.* **120**, 1161–1167 (2009).
38. X. Y. Ke, W. Hou, Q. Huang, X. Hou, X. Y. Bao, W. X. Kong, C. X. Li, Y. Q. Qiu, S. Y. Hu, L. H. Dong, Advances in electrical impedance tomography-based brain imaging. *Mil. Med. Res.* **9**, 10 (2022).
39. F.-R. Fan, Z.-Q. Tian, Z. Lin Wang, Flexible triboelectric generator. *Nano Energy* **1**, 328–334 (2012).
40. Z. L. Wang, Triboelectric nanogenerators as new energy technology and self-powered sensors – Principles, problems and perspectives. *Faraday Discuss.* **176**, 447–458 (2014).
41. J. Wang, C. Wu, Y. Dai, Z. Zhao, A. Wang, T. Zhang, Z. L. Wang, Achieving ultrahigh triboelectric charge density for efficient energy harvesting. *Nat. Commun.* **8**, 88 (2017).
42. Z. L. Wang, Triboelectric nanogenerator (TENG)—Sparking an energy and sensor revolution. *Adv. Energy Mater.* **10**, 2000137 (2020).
43. L. Zhang, H. Cai, L. Xu, L. Ji, D. Wang, Y. Zheng, Y. Feng, X. Sui, Y. Guo, W. Guo, F. Zhou, W. Liu, Z. L. Wang, Macro-superlubric triboelectric nanogenerator based on tribovoltaic effect. *Matter* **5**, 1532–1546 (2022).
44. X. Tao, X. Chen, Z. L. Wang, Design and synthesis of triboelectric polymers for high performance triboelectric nanogenerators. *Energ. Environ. Sci.* **16**, 3654–3678 (2023).
45. S. Yao, S. Wang, M. Zheng, Z. Wang, Z. Liu, Z. L. Wang, L. Li, Implantable, biodegradable, and wireless triboelectric devices for cancer therapy through disrupting microtubule and actins dynamics. *Adv. Mater.* **35**, e2303962 (2023).
46. X. Wei, Y. Wang, B. Tan, E. Zhang, B. Wang, H. Su, L. Yu, Y. Yin, Z. L. Wang, Z. Wu, Triboelectric nanogenerators stimulated electroacupuncture (EA) treatment for promoting the functional recovery after spinal cord injury. *Mater. Today* **60**, 41–51 (2022).
47. Q. Zhang, C. Xin, F. Shen, Y. Gong, Y. Zi, H. Guo, Z. Li, Y. Peng, Q. Zhang, Z. L. Wang, Human body IoT systems based on the triboelectrification effect: Energy harvesting, sensing, interfacing and communication. *Energ. Environ. Sci.* **15**, 3688–3721 (2022).
48. H. Ouyang, Z. Li, M. Gu, Y. Hu, L. Xu, D. Jiang, S. Cheng, Y. Zou, Y. Deng, B. Shi, W. Hua, Y. Fan, Z. Li, Z. Wang, A bioresorbable dynamic pressure sensor for cardiovascular postoperative care. *Adv. Mater.* **33**, e2102302 (2021).
49. H. Wang, J. Cheng, Z. Wang, L. Ji, Z. L. Wang, Triboelectric nanogenerators for human-health care. *Sci. Bull.* **66**, 490–511 (2021).
50. X. Peng, K. Dong, C. Ye, Y. Jiang, S. Zhai, R. Cheng, D. Liu, X. Gao, J. Wang, Z. L. Wang, A breathable, biodegradable, antibacterial, and self-powered electronic skin based on all-nanofiber triboelectric nanogenerators. *Sci. Adv.* **6**, eaba9624 (2020).
51. R. Wang, L. Mu, Y. Bao, H. Lin, T. Ji, Y. Shi, J. Zhu, W. Wu, Holistically engineered polymer–polymer and polymer–ion interactions in biocompatible polyvinyl alcohol blends for high-performance triboelectric devices in self-powered wearable cardiovascular monitorings. *Adv. Mater.* **32**, e2002878 (2020).
52. L. Lu, W. Chen, Biocompatible composite actuator: A supramolecular structure consisting of the biopolymer chitosan, carbon nanotubes, and an ionic liquid. *Adv. Mater.* **22**, 3745–3748 (2010).
53. L.-W. Lo, J. Zhao, K. Aono, W. Li, Z. Wen, S. Pizzella, Y. Wang, S. Chakrabartty, C. Wang, Stretchable sponge electrodes for long-term and motion-artifact-tolerant recording of high-quality electrophysiologic signals. *ACS Nano* **16**, 11792–11801 (2022).
54. M. Xia, J. Liu, B. J. Kim, Y. Gao, Y. Zhou, Y. Zhang, D. Cao, S. Zhao, Y. Li, J.-H. Ahn, Kirigami-structured, low-impedance, and skin-conformal electronics for long-term biopotential monitoring and human-machine interfaces. *Adv. Sci.* **11**, e2304871 (2024).
55. Y. Zhao, S. Zhang, T. Yu, Y. Zhang, G. Ye, H. Cui, C. He, W. Jiang, Y. Zhai, C. Lu, X. Gu, N. Liu, Ultra-conformal skin electrodes with synergistically enhanced conductivity for long-time and low-motion artifact epidermal electrophysiology. *Nat. Commun.* **12**, 4880 (2021).
56. B. Wei, Z. Wang, H. Guo, F. Xie, S. Cheng, Z. Lou, C. Zhou, H. Ji, M. Zhang, X. Wang, X. Jiao, S. Ma, H.-M. Cheng, X. Xu, Ultraflexible tattoo electrodes for epidermal and in vivo electrophysiological recording. *Cell Rep. Phys. Sci.* **4**, 101335 (2023).
57. Z. Vizvari, N. Gyorfi, A. Odry, Z. Sari, M. Klincsik, M. Gergics, L. Kovacs, A. Kovacs, J. Pal, Z. Karadi, Physical validation of a residual impedance rejection method during ultra-low frequency bio-impedance spectral measurements. *Sensors* **20**, 4686 (2020).
58. L. Pîslaru-Dănescu, G.-C. Zărnescu, G. Telipan, V. Stoica, Design and manufacturing of equipment for investigation of low frequency bioimpedance. *Micromachines* **13**, 1858 (2022).
59. V. S. Teixeira, W. Krautschneider, J. J. Montero-Rodríguez, in *2018 IEEE International Conference on Electrical Engineering and Photonics (EExPolytech)* (IEEE, 2018), pp. 147–151.
60. T. Faes, H. Van Der Meij, J. C. De Munck, R. M. Heethaar, The electric resistivity of human tissues (100 Hz-10 MHz): A meta-analysis of review studies. *Physiol. Meas.* **20**, R1–R10 (1999).
61. J. Latikka, H. Eskola, in *World Congress on Medical Physics and Biomedical Engineering 2018: June 3-8, 2018, Prague, Czech Republic (Vol. 1)* (Springer, 2019), pp. 773–776.
62. C. Gabriel, A. Peyman, E. H. Grant, Electrical conductivity of tissue at frequencies below 1 MHz. *Phys. Med. Biol.* **54**, 4863–4878 (2009).

Acknowledgment: We thank the patient C. H. Yu for assistance in TIT imaging. C. H. Yu is diagnosed with the lipoma in 2023 and, following treatment, has been gradually recovering. We also thank the patient Y. Li for help in TIT imaging. Y. Li is found to have microfractures on the ulna of his right arm in 2023 and has gradually recovered after treatment. We appreciate the contributions of X. Liu from Beijing University of Posts and Telecommunications Hospital and Z. Guo from Huaying Medical Company for assistance in clinical research. We also thank the Ethics Committee of Beijing Institute of Nanoenergy and Nanosystems for reviewing the experimental protocol documents. **Funding:** This work is supported by the National Natural Science Foundation of China for Excellent Yong Scholar (grant no. 52322313), National Natural Science Foundation of China (grant no. 62174014), Beijing Nova program (no. 20230484399), Youth Innovation Promotion Association CAS (2021165), Innovation Project of Ocean Science and Technology (22-3-3-hygg-18-hy), State Key Laboratory of New Ceramic and Fine Processing Tsinghua University (KFZD202202), Fundamental Research Funds for the Central Universities (292022000337), and Young Top-Notch Talents Program of Beijing Excellent Talents Funding (2017000021223ZK03). The recipient of all these funds is X.C. **Author contributions:** P.Y. and X.C. conceived the idea and supervised the experiment. P.Y., S.Q., and X.C. prepared the manuscript. P.Y. and Z.L.W. designed the structure of the device. P.Y. and S.Y. performed the data measurements. J.H. and Z.L. helped with the experiments. All authors discussed the results and commented on the manuscript. **Competing interests:** The authors declare that they have no competing interests. **Data and materials availability:** All data needed to evaluate the conclusions in the paper are present in the paper and/or the Supplementary Materials.

Submitted 21 July 2024
Accepted 15 November 2024
Published 20 December 2024
10.1126/sciadv.adr9139